

The effects of geometry on drift-limited solar cells

T. Kirkpatrick*, M. J. Burns, and M. J. Naughton

Department of Physics, Boston College, 140 Commonwealth Avenue, Chestnut Hill, Massachusetts 02467, USA

Received 21 June 2015, revised 15 March 2016, accepted 18 March 2016

Published online 9 May 2016

Keywords non-planar geometry, photovoltaics, radial nanowires, solar cells

* Corresponding author: e-mail kirkpatrick.lab@gmail.com

We present analytical simulations for the performance of nano-coaxial and -hemispherical drift-limited solar cells, to determine optimal geometrical configuration and to interpret results of experimental nanocoaxial solar cell arrays. The material system considered in these simulations is hydrogenated amorphous silicon (a-Si:H), with solar cells designed in an *n-i-p* stack. Simulations conducted for the performance of planar devices are compared against simulations performed

using SCAPS-1D and are found to be in close agreement. Simulation of the nanocoaxial array shows that while geometrical changes in the energy band diagram impact charge carrier collection, performance is most significantly impacted by light absorption properties associated with incident light interacting with the array of non-planar nanostructures. We compare our simulations to results of fabricated nanocoaxial a-Si:H solar cells.

© 2016 WILEY-VCH Verlag GmbH & Co. KGaA, Weinheim

1 Introduction Because single-crystal semiconductors can be expensive to produce [1–4], there has been a great deal of interest in producing solar cells from inexpensive thin film techniques [5–12], utilizing physical and/or chemical deposition methods. In addition to being comparatively inexpensive to produce, amorphous semiconductor absorption coefficients tend to be significantly larger than those of crystalline semiconductors across the majority of the visible spectrum [3, 6, 10–17], reducing the volume of material necessary to capture incident light, thereby further reducing the overall cost of solar cell fabrication. However, compared to crystalline materials, amorphous materials have little or no long-range atomic order and, in addition, often contain intrinsic defects, which tend to increase the density of trap states within the band gap. This has a compounded detrimental effect on the electrical properties [18–22] of amorphous materials by decreasing charge carrier mobility, and decreasing charge carrier lifetime τ_v .

One design criterion for maximizing efficiency of a-Si:H solar cells (as well as crystalline cells to a lesser extent) stems from the orientation of the photovoltaic junction with which the devices are fabricated; i.e., in a planar geometry. Because optical and electronic path lengths are, on average, collinear in planar geometries, the largest possible solar cell efficiencies occur for materials with electronic diffusion/

drift lengths that are much greater than average photon absorption depths [23]. Despite an enhancement in absorption over crystalline counterparts, amorphous materials do not fit this criterion [3, 5–14], which is indicative of just how low their μ_v and τ_v values are. However, non-planar solar cell geometries do not have collinear electronic and optical path lengths. Therefore, it is possible that by orthogonalizing these two path lengths using a non-planar architecture, solar cell efficiency may improve, despite low μ_v and τ_v values, by creating devices which are electrically “thin” in one direction and optically “thick” in another [24].

Previous work establishing a formal mathematical framework for analytically modeling geometrically generalized non-planar solar cells showed that device geometry and material properties are inextricably linked to overall solar cell performance [23]. Results qualitatively agreed with physical arguments about mutually orthogonal electronic and optical path lengths and, in addition, quantitatively showed that one design, in particular, significantly improved efficiency when using materials with properties that induce short electronic path lengths (i.e., low μ_v and τ_v) with respect to average absorption depths. For materials where the average absorption depth was smaller than, and even on the order of, the electronic diffusion/drift lengths, little improvement in efficiency was observed for non-planar geometries over the planar

geometry [23]. Therefore, amorphous materials represent an ideal material system to perform more detailed simulations in non-planar solar cell architectures. Here, performance of a-Si:H $n-i-p$ solar cells is simulated for comparison in planar, coaxial, and hemispherical designs (Fig. 1).

2 Theory The model [23] describing a generalized framework for analytically calculating non-planar solar cell architectures emphasized recombination rate variability in the space-charge region (SCR) (where the majority of the energy band bending occurs) as a function of geometry [23]. The i -layer thickness in a-Si:H solar cells is typically an order of magnitude larger than both the p - and n -layers, thereby dominating overall solar cell performance [3–5, 12]. For typical i -layer thicknesses used in a-Si:H solar cells (~ 100 nm), the entire i -layer is space-charge [4]. As such, this model [23] is well suited to study device performance of drift-limited solar cells in various geometrical configurations.

Because of relative layer thicknesses, the simulations for drift-limited solar cells performed here only emphasize i -layer drift transport, and neglect any diffusional transport from the p - and n -type quasi-neutral regions. As a validity check in making this approximation, in Fig. 2 device performance simulations for a *planar* a-Si:H solar cell are compared with ($p-i-n$) and without (i -layer only) diffusional charge transport contributions from the p - and n -layers. All simulation parameters are referred to in Table S1 of the Supporting Information. Results of the planar drift-limited device indicate that device performance of a-Si:H is negligibly impacted by quasi-neutral region transport, provided the i -layer is much thicker than the p - and n -layers; this is the basis for cells being called “drift-limited.” In these simulations, the ratios of $n:i:p$ layer thicknesses are held constant at 5:60:6 nm, and i -layer thickness is used as a batching parameter in the efficiency calculation of Fig. 2. In addition, in Fig. 2, simulations run for the planar cell are compared against a standard in amorphous material solar

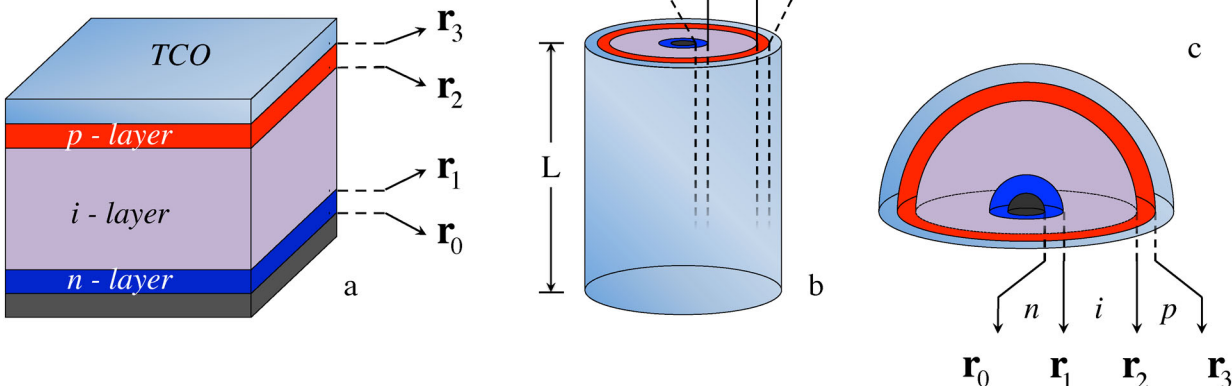


Figure 1 Architectures considered for a-Si:H, $n-i-p$ solar cells: (a) planar, (b) coaxial, and (c) hemispherical configuration.

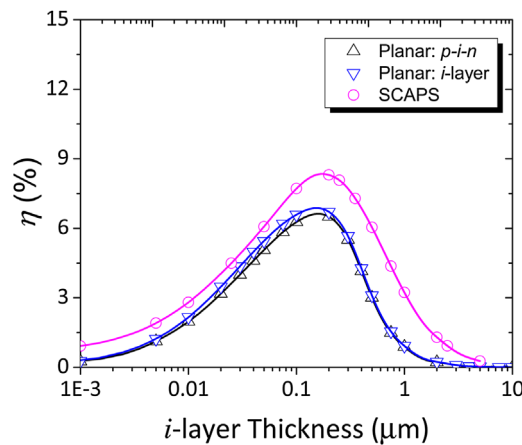


Figure 2 Efficiency curves for planar a-Si:H solar cells as a function of i -layer thickness. The results indicate that total device performance of planar a-Si:H solar cells is negligibly impacted by quasi-neutral region transport, provided that the i -layer is much thicker than the p - and n -layers. For these simulations, the ratio of $n:i:p$ layer thicknesses is held constant at 5:60:6 nm.

cell simulation, SCAPS-1D [25]. With comparable material parameters (e.g., band gap, layer thicknesses, doping levels, mobility, etc.) used here, SCAPS returns a similar efficiency curve; the primary difference being that efficiency values are slightly higher across the breadth of i -layer thicknesses (Fig. 2). For all planar a-Si:H $n-i-p$ solar cell simulations shown in Fig. 2, the peak efficiency occurs near an i -layer thickness of ~ 200 nm, with SCAPS predicting an efficiency approximately 1.5% (absolute) higher. It should be noted that SCAPS takes into account band-tail states, while these simulations do not. At the same time, simulations performed here include a charge collection probability within the i -layer, while SCAPS does not. The charge collection probability factor is meant to offset the lack of recombination from band tail states in a-Si:H. Both simulation techniques utilize mid-gap trap states for bulk

recombination in the *i*-layer, approximated to be the same energy level as the intrinsic chemical potential.

Unlike the planar geometry, where current conservation together with constant device cross section results in conservation of current *density*, in non-planar geometries, the non-constant device cross section results in only current being conserved. For any geometrical orientation of a photovoltaic junction aligned symmetrically along a single axis, the derived [23] contribution from the SCR to the total current of the device is given by the spatial volume integral of the generation and recombination rates over the SCR. For device performance simulations of a-Si:H solar cells, it is, again, noted that the *i*-layer is entirely space-charge. However, because amorphous materials are being simulated, to more accurately account for increased bulk recombination and imperfect charge carrier collection in the device, an *ad hoc* charge carrier collection probability factor $\psi(\mathbf{r}, V)$ is inserted into the expression for current,

$$i \approx i_{\text{SC}} = q \iiint [G_{\text{SC}}(\mathbf{r})\psi(\mathbf{r}, V) - U_{\text{SC}}(\mathbf{r})] d^3r.$$

The charge collection probability term $\psi(\mathbf{r}, V)$ does not affect the recombination (i.e., dark) current of the solar cell, and only impacts the light-generated current produced as a function of where in the *i*-layer the photon is absorbed. For all solar cell configurations, light is taken to be entering through the *p*-type window and/or along the *z*-axis. Solar cell area A_{PV} is set to 1 cm² for all devices. Expressions for space-charge solar cell current in planar, coaxial, and hemispherical architectures are discussed in detail in Ref. [23], and are reproduced in Table S2 of the Supporting Information.

The bulk recombination rate $U_{\text{SC}}(\mathbf{r})$ used in these calculations is a sum of radiative, Shockley-Reade-Hall (SRH), and Auger recombination in the SCR, as explained in Ref. [23]. Band tail and surface recombination are not included in the analysis, nor is a potential difference from the electrodes. The spatial dependence for all recombination is expressed implicitly in the intrinsic chemical potential $\mu_i(\mathbf{r})$. The spatial dependence of $\mu_i(\mathbf{r})$ is also discussed in [23]. Functional expressions for the generation rates in the *i*-layer are reproduced in Table S3 of the Supporting Information. The upper limit for integration is a function of applied bias V , given by the expression $\varepsilon_{\text{max}}(V) = \chi_{\text{SC}} - \Delta_{\text{SC}} - V$, where Δ_{SC} is the band gap and χ_{SC} is the electron affinity in the *i*-layer. To reduce computation time in simulations, the upper limit in the integral calculations is approximated to be $\varepsilon_{\text{max}} = \chi_{\text{SC}} - \Delta_{\text{SC}}$.

Because the *i*-layer does not contain majority or minority charge carriers, the probability of extraction for both electrons and holes should be accounted for with the collection probability term; i.e., $\psi(\mathbf{r}, V) = \psi_e(\mathbf{r}, V) + \psi_h(\mathbf{r}, V)$. The individual charge carrier collection decays exponentially away from the region where electrons and holes are collected, respectively, modulated by the drift lengths $\mathbf{l}_{v=e,h}(\mathbf{r}, V)$ in the *i*-layer [26–28]. After charge carriers are photogenerated in the *i*-layer, electrons are collected at the *n*-layer contact, and holes at the *p*-layer contact. Because the generation

rate describes generated electron-hole pairs, the extraction probability, used here in conjunction with the generation rate that defines the light-current produced, must account for the probability of extracting both charge carrier types. Therefore, the sum of electron and hole collection probabilities in the *i*-layer can never be greater than one; i.e.,

$$\psi(\mathbf{r}, V) = \psi_e(\mathbf{r}, V) + \psi_h(\mathbf{r}, V)$$

$$= A \exp\left(-\frac{\mathbf{r} - \mathbf{r}_1}{\mathbf{l}_e(\mathbf{r}, V)}\right) + B \exp\left(\frac{\mathbf{r} - \mathbf{r}_2}{\mathbf{l}_h(\mathbf{r}, V)}\right) \leq 1,$$

where A and B are coefficients/decay amplitudes to be determined. Because electrons are collected at the *n*-layer contact, for an electron-hole pair photogenerated at, the probability that the electron will be collected is one. To account for the collection probability of both charge carrier types associated with the photogenerated current in this model, it is, therefore, approximated that the sum of electron and hole collection probabilities at \mathbf{r}_1 is 1, i.e.,

$$\psi(\mathbf{r}, V)|_{\mathbf{r}=\mathbf{r}_1} = \psi_e(\mathbf{r}, V)|_{\mathbf{r}=\mathbf{r}_1} + \psi_h(\mathbf{r}, V)|_{\mathbf{r}=\mathbf{r}_1}$$

$$= A + B \exp\left(\frac{\mathbf{r}_1 - \mathbf{r}_2}{\mathbf{l}_h(\mathbf{r}_1, V)}\right) = 1.$$

It is important to re-emphasize that the recombination rate across the *i*-layer will account for dark-current produced in this model, and the collection probability only accounts for a reduction in the photogenerated current produced. Likewise, for an electron-hole pair photogenerated at, the probability that the hole will be collected must be 1, and therefore

$$\psi(\mathbf{r}, V)|_{\mathbf{r}=\mathbf{r}_2} = \psi_e(\mathbf{r}, V)|_{\mathbf{r}=\mathbf{r}_2} + \psi_h(\mathbf{r}, V)|_{\mathbf{r}=\mathbf{r}_2}$$

$$= A \exp\left(-\frac{\mathbf{r}_2 - \mathbf{r}_1}{\mathbf{l}_e(\mathbf{r}_2, V)}\right) + B = 1.$$

Solving for the coefficients A and B ,

$$A = \frac{1 - \exp\left(\frac{\mathbf{r}_2 - \mathbf{r}_1}{\mathbf{l}_h(\mathbf{r}_1, V)}\right)}{\exp\left(\frac{\mathbf{r}_1 - \mathbf{r}_2}{\mathbf{l}_e(\mathbf{r}_2, V)}\right) - \exp\left(\frac{\mathbf{r}_2 - \mathbf{r}_1}{\mathbf{l}_h(\mathbf{r}_1, V)}\right)}$$

and

$$B = \frac{\exp\left(\frac{\mathbf{r}_2 - \mathbf{r}_1}{\mathbf{l}_e(\mathbf{r}_2, V)}\right) - 1}{\exp\left(\frac{\mathbf{r}_2 - \mathbf{r}_1}{\mathbf{l}_e(\mathbf{r}_2, V)}\right) - \exp\left(\frac{\mathbf{r}_1 - \mathbf{r}_2}{\mathbf{l}_h(\mathbf{r}_1, V)}\right)}.$$

Note: the coefficients are a function of the applied voltage V . The charge carrier drift lengths $\mathbf{l}_{v=e,h}(\mathbf{r}, V)$ modulating collection in the *i*-layer are expressed in terms of the electric field $\mathbf{E}(\mathbf{r}, V)$ as $\mathbf{l}_{v=e,h}(\mathbf{r}, V) = \mu_v \tau_v \mathbf{E}(\mathbf{r}, V)$. Based on approximate energy band diagram profiles [23],

the electric fields in the SCR for the planar, coaxial, and hemispherical geometries are given in Table S3 of the Supporting Information. Details of the energy band profiles used for non-planar architectures are discussed in detail in Ref. [23].

Using ellipsometry data to define the real $n(\varepsilon_\gamma)$ and imaginary $k(\varepsilon_\gamma)$ indices of refraction for a-Si:H [29], the absorption coefficient $\alpha(\varepsilon_\gamma)$ is calculated via the relationship $\alpha(\varepsilon_\gamma) = 4\pi k(\varepsilon_\gamma) [\lambda(\varepsilon_\gamma)^{-1}]$, which is used in the equations in Tables S2 and S3 of the Supporting Information to calculate the light-current produced for each structure. The 2D hcp lattice for the non-planar structures, which also affects the light-current produced, is shown in Fig. 3. From observation of the 2D hcp lattice, it is seen that some light incident on the array will be lost in the empty space between adjacent cells. The percentage of available area for photovoltaic conversion will vary as a function of the radial size of individual cells. That is, for increasingly thinner i -layers in the coaxial and hemispherical arrays, the percentage of empty space in between individual cells decreases.

In these simulations, solar cell performance is considered under conditions of light concentration (for the non-planar structures). Concern for simulations incorporating light concentration stem from the fact that when spacing (i.e., pitch) between adjacent non-planar cells has sub-wavelength dimensions, the inner metallic contacts can act as optical antennae [30–32], thereby harvesting more light, and consequently increasing short-circuit current produced. Two limits are considered: (i) when there is no light concentration, and thus any incident light on the empty space between individual cells is lost and (ii) perfect light concentration, when all incident light on the array is focused into the active photovoltaic area.

This will, therefore, yield upper and lower limits for performance of such arrays. The case of perfect light concentration is treated by conserving incident photon

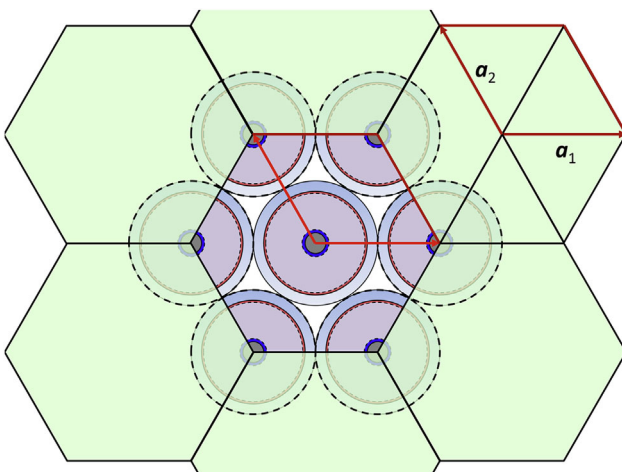


Figure 3 2D hcp array of nanoscopic coaxial/hemispherical solar cells.

flux $I_{AM1.5}(\varepsilon_\gamma) [\varepsilon_\gamma^{-1}]$ on the primitive cell into the annulus of individual non-planar cells. Doing so causes photon flux intensity in the annulus to be larger than the actual incident photon flux intensity, since the area of the annulus is smaller than the area of the primitive cell. The increased intensity of the spectral irradiance in the annulus is given by

$$I_{AM1.5+}(\varepsilon_\gamma) = I_{AM1.5}(\varepsilon_\gamma) \frac{2r_1^2\sqrt{3}}{\pi[r_3^2 - r_0^2]},$$

where $I_{AM1.5}$ is the solar spectrum incident onto the primitive cell, $I_{AM1.5+}$ is the solar spectrum that is concentrated into the annulus, the area of the primitive cell is $2r_1^2\sqrt{3}$, and the area of the annulus of the non-planar cell is $\pi[r_3^2 - r_0^2]$. This concentrated spectrum replaces the AM1.5 spectrum in Table S2 of the Supporting Information, when simulating performance under perfect light concentration conditions. The number N of cells in the array is determined from the primitive cell area by $N = A_{PV}/(2r_1^2\sqrt{3})$, where, again, $A_{PV} = 1 \text{ cm}^2$ for all simulations. Under light concentrating conditions, the performance of a non-planar array behaves as though the number of cells in the array were increased. This can be seen by multiplying the concentrated solar spectrum with the number of cells in the array; i.e.,

$$NI_{AM1.5+}(\varepsilon_\gamma) = \frac{A_{PV}}{\pi[r_3^2 - r_0^2]} I_{AM1.5}(\varepsilon_\gamma).$$

Hence, the multiplication of the concentrated spectrum and number of cells in the array can be equally described as an effective number of cells in the array $N_{eff} = A_{PV}/(\pi[r_3^2 - r_0^2])$ multiplied by the normal AM1.5 solar spectrum; i.e., $NI_{AM1.5+}(\varepsilon_\gamma) = N_{eff} I_{AM1.5}(\varepsilon_\gamma)$.

3 Results and discussion From the spatially dependent behavior of the electric fields for the non-planar structures, it is seen that charge carrier drift lengths $\mathbf{l}_v(\mathbf{r}, V)$ decay with respect to the inner most charge collecting region which, in turn, will affect the charge collection probability for each charge carrier type. Figure 4 shows how charge carrier collection decreases with increasing i -layer thickness. The coaxial architecture collects charge more efficiently for thicker i -layers, as indicated in Fig. 4b and c, however, this result will change for varying inner radii \mathbf{r}_0 values used in the calculations; the initial electric field intensity at \mathbf{r}_1 will vary as \mathbf{r}_0 varies, for both the coaxial and hemispherical structures. The asymmetry in the planar charge carrier collection probability (the planar electric field is approximated as constant) arises from the difference in drift lengths for electrons and holes, due to the two-order of magnitude lower hole mobility associated with intrinsic a-Si:H [3, 5–9, 12–14, 18–22, 26]. Because of this, for thicker i -layers, the probability of hole collection is extremely low, except when electron-hole pairs are photo-generated very near the p -layer interface (Fig. 4a). For the non-planar architectures this asymmetry is compounded

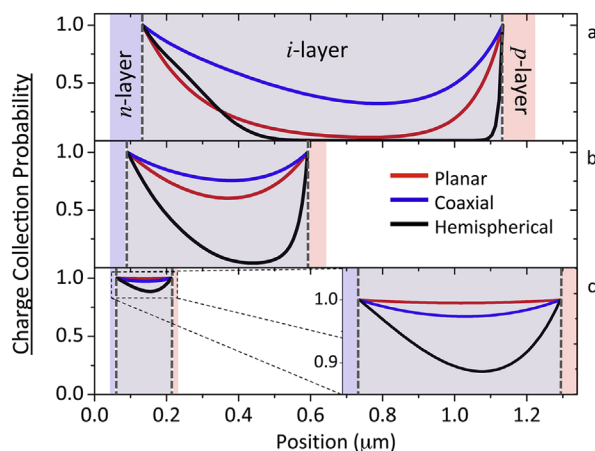


Figure 4 Charge carrier collection probabilities within the *i*-layer for planar (red), coaxial (blue), and hemispherical (black) a-Si:H solar cells, for *i*-layer thicknesses of (a) 1000 nm, (b) 500 nm, and (c) 150 nm.

because, in addition to shorter hole drift-lengths, the electric field decays in intensity from \mathbf{r}_1 as ρ^{-1} and r^{-2} for the coaxial and hemispherical structures, respectively.

By varying coaxial length in the simulations, optimal coaxial performance occurs near a length of 10 μm , under both normal and light concentrating conditions. Figure 5 shows all three structures plotted versus *i*-layer thickness, with the coaxial plots having lengths of 10 μm . Spanning all *i*-layer thicknesses, the coaxial structure outperforms both the planar and the hemispherical architectures, with a peak efficiency lying at just over 12%. However, the coaxial architecture only outperforms the planar architecture when including perfect light concentration into the model. Because of light concentrating affects, the coaxial structure is most efficient when *i*-layer thickness is small (the

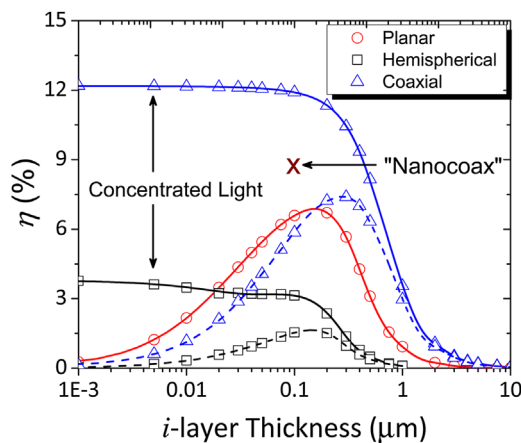


Figure 5 Efficiency versus *i*-layer thickness curves. The dashed lines represent the efficiency curves when less than 100% light absorption occurs for the coaxial and hemispherical structures. The “ \times ” marks the location of the efficiency observed experimentally [24] for the nanocoax in 2010.

efficiency plateaus for *i*-layer thicknesses less than or equal to 100 nm), when charge carrier extraction is maximized. When the coaxial array has no light concentrating effects, it performs similar to the planar device. Experimentally, it could be expected that the coaxial array would perform somewhere between the two limits of concentration considered here, since perfect light concentration is unrealistic in a real device.

Based on values for maximum efficiency calculated in these simulations, geometrical variations of the energy band diagram in the SCR do not appear to be affecting solar cell performance significantly. For all simulations performed, with and without light concentration, optimal *i*-layer thicknesses occur near or below values where charge carrier collection begins to degrade (compare collection probabilities with *i*-layer thicknesses in Fig. 4). Therefore, while geometrical changes to the energy band diagram most certainly affect charge transport in the SCR, it is the effect that the sub-wavelength pitch of the array has on light harvesting that seems to be most significantly impacting performance from the planar to non-planar architecture.

I–*V* curves representative of maximum efficiency are shown in Fig. 6. The *i*-layer thicknesses used are 150 nm for the planar, 5 nm for the coaxial, and 5 nm for the hemispherical, as these are the approximate optimal spatial parameters that maximize efficiency in each structure. Comparison between experimentally-fabricated planar and nanocoaxial a-Si:H solar cells was reported in 2010 [24]. In this study, it was observed that efficiency improvement for the nanocoaxial array arose from enhanced absorption properties associated with these devices; even greater than those observed for textured and back reflector superstrate a-Si:H solar cells [24]. For the planar a-Si:H solar cell reported in that study, the short-circuit current value obtained is nearly identical to the value obtained using

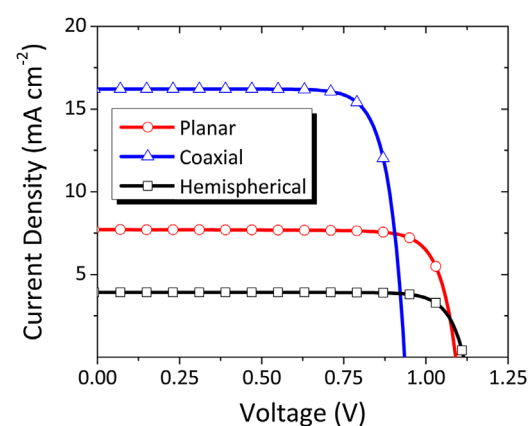


Figure 6 *I*–*V* curves for optimized spatial parameters within each geometry, performed over an area of 1 cm^2 . The *i*-layer thicknesses are 150 nm for the planar, 5 nm for the coaxial, and 5 nm for the hemispherical structures. The coaxial structure is 10 μm long. The *I*–*V* curves shown represent current under 100% light absorption.

this simulation (Fig. 6). It is noted that in Ref. [24], the *i*-layer thickness of the planar cell was 90 nm, while the *I*–*V* trace referred to in Fig. 6 has an *i*-layer thickness of 150 nm. However, according to Fig. 5, performance of the planar architecture will not change appreciably between *i*-layer thicknesses of 90–200 nm, due to the breadth of the efficiency peak; hence short-circuit current for the planar architecture will be nearly identical when *i*-layer thickness is 90 nm. Similarly, short-circuit current observed for the nanocoaxial array very closely resembles the maximum short-circuit current observed in the simulations performed here. Again, an important distinction between the two is that *i*-layer thickness and length of the nanocoax in Ref. [24] were 90 nm and 1.5 μm , respectively, while the *i*-layer thickness and length of the nanocoaxial array in Fig. 6 are 5 nm and 10 μm , respectively. As with the comparison between the planar cell in Ref. [24] and the simulations performed here, the calculated efficiency for the nanocoaxial array does not change appreciably when *i*-layer thickness is less than 100 nm. As such, the efficiency calculated when *i*-layer thickness is 5 nm will be nearly identical as when *i*-layer thickness is 90 nm.

For all simulations performed, the open-circuit voltage for each structure exceeds those reported in Ref. [24]. This is accredited to other forms of recombination not included; namely band tail recombination. The fact that additional forms of recombination were not included in the simulation was the motivation for including the charge collection probability term in the expression for total current. While the charge collection term more closely aligns the values for short-circuit current, as compared to experimental values, it does not affect the open-circuit voltages calculated, which is the reason why the open-circuit voltages achieved exceed those reported experimentally. Excluding band tail recombination, the open-circuit voltages obtained seem perfectly acceptable compared to experimental values. The lower open-circuit voltage observed for the nanocoaxial cell arises from the increase in dark (i.e., saturation) current, as a result of the larger *i*-layer volume in this geometry (the nanocoaxial length is 10 μm). Saturation current increases proportional to volume of material, while photogenerated current increases proportional to the area of the cell.

The efficiency reported for the nanocoax in Ref. [24] is approximately 8%, which lies directly between the two limits of light concentration considered in these simulations (Fig. 5). Therefore, these simulations closely match the experimental results for both the planar and nanocoax a-Si:H solar cells reported in Ref. [24], and provide evidence that the sub wavelength pitch of the array is the root cause for the enhanced short-circuit current observed experimentally in the nanocoax a-Si:H solar cell.

The simulations performed herein utilize an analytical model [23] describing the geometrically generalized device physics of *p*–*n* junctions. However, due to the drift-limited nature of a-Si:H solar cells, only a subsection of that model was used here; i.e., the generalized description in the SCR.

For thin film solar cells in other material systems (e.g., CdTe, CIGS, etc.), which are not dominated by charge drift, it will be necessary to include diffusional charge transport from the doped quasi-neutral regions to accurately model their performance. Although not discussed in this work, solutions for diffusional charge transport will entail numerically solving non-linear, inhomogeneous, partial differential equations when working in cylindrically or spherically symmetric geometries. By combining the solutions for diffusional transport from the quasi-neutral regions with the drift transport from the SCR, a *p*–*n* junction solar cell constructed in any symmetrical geometry, in any material system, can be mathematically modeled using this generalized formalism.

4 Conclusions We have simulated performance for drift-limited a-Si:H *n*–*i*–*p* solar cells in planar, coaxial, and hemispherical architectures. Our simulations provide evidence for the drift-limited nature of a-Si:H *n*–*i*–*p* device performance. In addition, our simulations for the planar device are in good agreement with other simulation platforms (i.e., SCAPS-1D). Our simulations show that efficiency improvements are possible for the coaxial architecture only when taking into account light concentrating effects from the sub wavelength pitch of the array. The increased short-circuit current of the nanocoax architecture stems from enhanced light absorption, not from enhanced charge collection due to changes in the built-in electric field as a function of geometry. Performance of the nanocoaxial a-Si:H solar cell, calculated in this simulation, closely resembles that reported in 2010 and provides evidence to the nature of increased short-circuit current and absorption observed experimentally.

Supporting Information Additional supporting information may be found in the online version of this article at the publisher's web-site.

Acknowledgments The authors would like to thank Dr. Constantin Andronache at Boston College for useful conversations regarding the setup of these simulations. The authors would also like to thank Prof. Nikolas Podraza, University of Toledo, for performing ellipsometry on films grown at Solasta Inc.

References

- [1] D. M. Powell, M. T. Winkler, A. Goodrich, and T. Buonassisi, Modeling the Cost and Minimum Sustainable Price of Crystalline Silicon Photovoltaic Manufacturing in the United States, *IEEE J. Photovolt.* **3**(2), 662–668 (2013).
- [2] A. Shah, P. Torres, R. Tscharner, N. Wyrsch, and H. Keppner, Photovoltaic Technology: The Case for Thin-Film Solar Cells, *Science* **285**(5428), 692–698 (1999).
- [3] R. E. I. Schropp and M. Zeman, *Amorphous and Microcrystalline Silicon Solar Cells: Modeling, Materials, and Device Technology* (Kluwer Academic, Boston, 1998).
- [4] J. Nelson, *The Physics of Solar Cells* (Imperial College Press, London, 2003).

- [5] P. G. Le Comber and W. E. Spear, Electronic Transport in Amorphous Silicon Films, *Phys. Rev. Lett.* **25**(8), 509–511 (1970).
- [6] W. Fuhs, M. Milleville, and J. Stuke, Drift Mobility and Photoconductivity in Amorphous Silicon, *Phys. Status Solidi B* **89**(2), 495–502 (1978).
- [7] A. R. Moore, Electron and Hole Drift Mobility in Amorphous Silicon, *Appl. Phys. Lett.* **31**(11), 762 (1977).
- [8] T. Tiedje, C. R. Wronski, B. Abeles, and J. M. Cebulka, Electron Transport in Hydrogenated Amorphous Silicon: Drift Mobility and Junction Capacitance, *Sol. Cells* **2**(3), 301–318 (1980).
- [9] C. R. Wronski, D. E. Carlson, R. E. Daniel, and A. R. Triano, Electrical Properties of a-Si Solar Cells, International Electron Devices Meeting (1976), pp. 75–78.
- [10] D. E. Carlson, Amorphous Silicon Solar Cells, *IEEE Trans. Electron Devices* **24**(4), 449–453 (1977).
- [11] D. E. Carlson and C. R. Wronski, Amorphous Silicon Solar Cell, *Appl. Phys. Lett.* **28**(11), 671–673 (1976).
- [12] H. Okamoto, Y. Nitta, T. Yamaguchi, and Y. Hamakawa, Device Physics and Design of a-Si ITO/p-i-n Heteroface Solar Cells, *Sol. Energy Mater. Sol. Cells* **2**, 313–325 (1980).
- [13] R. Konenkamp, Transport in a-Si:H and Its Alloys (Springer-Verlag, Berlin, Heidelberg, 2000), Chapter 3.
- [14] E. A. Schiff, Transport, Interfaces, and Modeling in Amorphous Silicon Based Solar Cells, Subcontract Report DOE NREL/SR-520-44101 (2008).
- [15] P. Tzanetakis, H. Fritzsch, M. Q. Tran, M. Androulidaki, and E. Rynes, Photoconductivity in Compensated a-Si:H and the Effect of Bias Light on the Drift Mobility, *J. Non-Cryst. Solids* **164**, 607–610 (1993).
- [16] A. Luque and S. Hegedus, Handbook of Photovoltaic Science and Engineering (Wiley, Chichester, West Sussex, UK, 2011).
- [17] S. J. Fonash, Solar Cell Device Physics, 2nd edn. (Academic Press/Elsevier, Burlington, MA, 2010).
- [18] E. A. Schiff, Transit Time Measurements of Charge Carriers in Disordered Silicons: Amorphous, Microcrystalline, and Porous, *Philos. Mag.* **89**(28–30), 2505–2518 (2009).
- [19] R. Schwarz, F. Wang, and S. Grebner, Diffusion, Drift, and Recombination of Holes in a-Si:H, *Mater. Res. Soc. Symp. Proc.* **377**, 427–436 (1995).
- [20] E. A. Schiff, Hole Mobilities and the Physics of Amorphous Silicon Solar Cells, *J. Non-Cryst. Solids* **352**(9), 1087–1092 (2006).
- [21] J. Liang, E. A. Schiff, S. Guha, B. Yan, and J. Yang, Hole-Mobility Limit of Amorphous Silicon Solar Cells, *Appl. Phys. Lett.* **88**(6), 063512 (2006).
- [22] R. Street, J. Kakalios, and M. Hack, Electron Drift Mobility in Doped Amorphous Silicon, *Phys. Rev. B* **38**(8), 5603–5609 (1988).
- [23] T. Kirkpatrick, M. J. Burns, and M. J. Naughton, Analytical Device-Physics Framework for Non-Planar Solar Cells, *Sol. Energy Mater. Sol. Cells* **133**, 229–239 (2015).
- [24] M. J. Naughton, K. Kempa, Z. F. Ren, Y. Gao, J. Rybczynski, N. Argenti, W. Gao, Y. Wang, Y. Peng, J. R. Naughton, G. McMahon, T. Paudel, Y. C. Lan, M. J. Burns, A. Shepard, M. Clary, C. Ballif, F. J. Haug, T. Söderström, O. Cubero, and C. Eminian, Efficient Nanocoax-Based Solar Cells, *Phys. Status Solidi RRL* **4**(7), 181–183 (2010).
- [25] M. Burgelman, J. Verschraegen, S. Degrave, and P. Nollet, Modeling Thin-Film PV Devices, *Prog. Photovolt.* **12**(2), 143–153 (2004).
- [26] K. Kempa, M. J. Naughton, Z. F. Ren, A. Herczynski, T. Kirkpatrick, J. Rybczynski, and Y. Gao, Hot Electron Effect in Nanoscopically Thin Photovoltaic Junctions, *Appl. Phys. Lett.* **95**, 233121 (2009).
- [27] C. Donolato, Reconstruction of the Charge Collection Probability in a Solar Cell from Internal Quantum Efficiency Measurements, *J. Appl. Phys.* **89**(10), 5687–5695 (2001).
- [28] F. Galluzzi, Photogenerated Carrier Collection in Semiconductors with Low Mobility-Lifetime Products, *J. Phys. D, Appl. Phys.* **18**(4), 685–689 (1985).
- [29] Ellipsometry performed by Prof. Nikolas Podraza, University of Toledo, on films grown at Solasta Inc.
- [30] P. Bharadwaj and B. Deutscher, Optical Antennas, *Adv. Opt. Photon.* **1**, 438–483 (2009).
- [31] P. Krogstrup, H. I. Jørgensen, M. Heiss, O. Demichel, J. V. Holm, M. Aagesen, J. Nygard, and A. Fontcuberta i Morral, Single-Nanowire Solar Cells Beyond the Shockley–Queisser Limit, *Nature Photon.* **7**(4), 306–310 (2013).
- [32] H. A. Atwater and A. Polman, Plasmonics for Improved Photovoltaic Devices, *Nature Mater.* **9**(3), 205–213 (2010).

Supporting Information for:

The effects of geometry on drift-limited solar cells

[Phys. Status Solidi B, DOI 10.1002/pssb.201552412 (2016)]

T. Kirkpatrick*, M. J. Burns, and M. J. Naughton

Department of Physics, Boston College, 140 Commonwealth Avenue, Chestnut Hill, Massachusetts 02467, USA

Received 21 June 2015, revised 15 March 2016, accepted 18 March 2016
Published online April 2016

Keywords non-planar geometry, radial nanowires, solar cells, photovoltaics

* Corresponding author: e-mail kirkpatrick.lab@gmail.com

Table S1. Simulation parameter values.

Symbol	Values
q	Fundamental unit of charge 1.602×10^{-19} [C]
\hbar	Planck's constant 1.055×10^{-34} [J s]
k_B	Boltzmann's constant 1.38×10^{-23} [J K ⁻¹]
c	Speed of light in vacuum 3.0×10^{10} [cm s ⁻¹]
T_A	Ambient temperature of solar cell 300 [K]
β_A	Inverse thermal energy of ambient temperature $(k_B T_A)^{-1}$ [J ⁻¹]
N_C	Conduction band effective density of states 2.5×10^{20} [cm ⁻³]
N_V	Valence band effective density of states 2.5×10^{20} [cm ⁻³]

N_D	Concentration of donor atoms/free electrons in n-type region	$8.0 \times 10^{18} \text{ [cm}^{-3}]$
N_A	Concentration of acceptor atoms/free holes in p-type region	$3.0 \times 10^{18} \text{ [cm}^{-3}]$
Δ_{SC}	Band gap of intrinsic amorphous silicon	1.7 [eV]
n_i	Intrinsic charge carrier concentration in i -layer	$\sqrt{N_C N_V} \exp\left(-\beta_A \frac{\Delta_{SC}}{2}\right) \text{ [cm}^{-3}]$
t_M	Thickness of TCO window	$50.0 \times 10^{-7} \text{ [cm]}$
r_0	Thickness of back contact/origin offset	$50.0 \times 10^{-7} \text{ [cm]}$
t_{SC}	Thickness of i -layer/space-charge region	Batching parameter [cm]
$t_N(t_{SC})$	Thickness of n-type region	$\frac{t_{SC}}{12} \text{ [cm]}$
$t_P(t_{SC})$	Thickness of p-type region	$\frac{t_{SC}}{10} \text{ [cm]}$
$r_1(t_{SC})$	n -type region edge	$r_0 + t_N(t_{SC}) \text{ [cm]}$
$r_2(t_{SC})$	Space-charge region edge	$r_1(t_{SC}) + t_{SC} \text{ [cm]}$
$r_3(t_{SC})$	p -type region edge	$r_2(t_{SC}) + t_P(t_{SC}) \text{ [cm]}$
$r_4(t_{SC})$	Front surface of cell	$r_3(t_{SC}) + t_M \text{ [cm]}$
ε_γ	Photon energy	Integration variable [J]
$\lambda(\varepsilon_\gamma)$	Photon wavelength	$\frac{2\pi\hbar c}{\varepsilon_\gamma} \text{ [cm]}$
A_{PV}	Area of solar cell	1.0 [cm ²]

N	Number of solar cells	$\frac{A_{PV}}{2 r_4(t_{SC})^2 \sqrt{3}}$
N_{eff}	Effective number of solar cells under light concentration	$\frac{A_{PV}}{\pi [r_3(t_{SC})^2 - r_0^2]}$
χ_{SC}	Electron affinity in i -layer	3.9 [eV]
V	Applied bias	Independent variable [V]
$\varepsilon_{\max}(V)$	Maximum absorbed photon energy	$\chi_{SC} + \Delta_{SC} - V$ [eV]
μ_n	Electron mobility in i -layer	1.0 [$\text{cm}^2 \text{V}^{-1}\text{s}^{-1}$]
μ_p	Hole mobility in i -layer	0.01 [$\text{cm}^2 \text{V}^{-1}\text{s}^{-1}$]
τ_n	Electron lifetime in i -layer	1.0×10^{-9} [s]
τ_p	Hole lifetime in i -layer	5.0×10^{-9} [s]
Λ_n	Electron Auger recombination coefficient in i -layer	0.3×10^{-30} [cm^6s^{-1}]
Λ_p	Hole Auger recombination coefficient in i -layer	1.1×10^{-30} [cm^6s^{-1}]
B	Radiative recombination coefficient	1.1×10^{-14} [cm^3s^{-1}]
V_{BI}	Built-in junction bias	$\frac{1}{q \beta_A} \ln \left(\frac{N_D N_A}{n_i^2} \right)$ [V]

Table S2. Expressions for a-Si:H current for planar, coaxial, and hemispherical structures.

Geometry	Total Current Expression
Planar	$i = qA_{PV} \int_{r_1}^{r_2} [G_{SC}(z)\psi(z) - U_{SC}(z)] dz$
Coaxial	$i = qN \iiint_{r_1}^{r_2} [G_{SC}(z)\psi(\rho) - U_{SC}(\rho)] \rho d\rho d\phi dz$
Hemispherical	$i = qN \iiint_{r_1}^{r_2} [G_{SC}(r, \theta)\psi(r) - U_{SC}(r)] r^2 \sin(\theta) dr d\theta d\phi$

Table S3. Functional expressions for generation rates with longitudinal light incidence $\hat{k} = -\hat{z}$, and approximate electric fields in the SCR in planar, coaxial, and hemispherical geometries.

Geometry	Generation rate: $G_{SC}(\vec{r})$	Approximate Electric field: $E(\vec{r}, V)$
Planar $\hat{k} = -\hat{z}$	$\int_{\Delta_{SC}}^{\varepsilon_{\max}(V)} \frac{I_{AM1.5}(\varepsilon_\gamma)}{\varepsilon_\gamma} \alpha(\varepsilon_\gamma) \exp(-\alpha(\varepsilon_\gamma)[r_3 - z]) d\varepsilon_\gamma$	$\frac{[V_{BI} - V]}{r_2 - r_1}$
Coaxial $\hat{k} = -\hat{z}$	$\int_{\Delta_{SC}}^{\varepsilon_{\max}(V)} \frac{I_{AM1.5}(\varepsilon_\gamma)}{\varepsilon_\gamma} \alpha(\varepsilon_\gamma) \exp(-\alpha(\varepsilon_\gamma)[L - z]) d\varepsilon_\gamma$	$\frac{[V_{BI} - V]}{\rho} \ln\left(\frac{r_2}{r_1}\right)$
Hemispherical $\hat{k} = -\hat{z}$	$\cos^2(\theta) \int_{\Delta_{SC}}^{\varepsilon_{\max}(V)} \frac{I_{AM1.5}(\varepsilon_\gamma)}{\varepsilon_\gamma} \alpha(\varepsilon_\gamma) \exp(-\alpha(\varepsilon_\gamma)[r_3 - r] \cos(\theta)) d\varepsilon_\gamma$	$\frac{[V_{BI} - V]}{r^2} \left[\frac{r_1 r_2}{r_2 - r_1} \right]$